PNAS RESEARCH ARTICLE | PHARMACOLOGY

Cooperative regulation of coupled oncoprotein synthesis and stability in triple-negative breast cancer by EGFR and CDK12/13

Hazel X. Ang[a,1], Natalia Sutiman[b], Xinyue L. Deng[a], Annie Liu[a,c], Christian G. Cerda-Smith[a], Haley M. Hutchinson[a], Holly Kim[a], Luke C. Bartelt[d], Qiang Chen[e], Alejandro Barrera[d,f], Jiaxing Lin[g], Zhecheng Sheng[g], Ian C. McDowell[d,f], Timothy E. Reddy[d,f], Christopher V. Nicchitta[e,2], and Kris C. Wood[a,2]

Edited by Joan Brugge, Harvard Medical School, Boston, MA; received January 11, 2023; accepted July 19, 2023

Evidence has long suggested that epidermal growth factor receptor (EGFR) may play a prominent role in triple-negative breast cancer (TNBC) pathogenesis, but clinical trials of EGFR inhibitors have yielded disappointing results. Using a candidate drug screen, we identified that inhibition of cyclin-dependent kinases 12 and 13 (CDK12/13) dramatically sensitizes diverse models of TNBC to EGFR blockade. This combination therapy drives cell death through the 4E-BP1-dependent suppression of the translation and translation-linked turnover of driver oncoproteins, including MYC. A genome-wide CRISPR/Cas9 screen identified the CCR4-NOT complex as a major determinant of sensitivity to the combination therapy whose loss renders 4E-BP1 unresponsive to drug-induced dephosphorylation, thereby rescuing MYC translational suppression and promoting MYC stability. The central roles of CCR4-NOT and 4E-BP1 in response to the combination therapy were further underscored by the observation of CNOT1 loss and rescue of 4E-BP1 phosphorylation in TNBC cells that naturally evolved therapy resistance. Thus, pharmacological inhibition of CDK12/13 reveals a long-proposed EGFR dependence in TNBC that functions through the cooperative regulation of translation-coupled oncoprotein stability.

CDK12/13 | EGFR | triple-negative breast cancer | MYC | protein quality control

Triple-negative breast cancer (TNBC) is an aggressive subtype of the disease that constitutes 15 to 20% of all breast cancers. TNBCs are clinically defined by their lack of expression of the three main targetable receptors in breast cancer—the estrogen (ER), progesterone (PR), and human epidermal growth receptor-2 (HER2) receptors. The genetic and molecular heterogeneity within this pooled disease subtype has made patient stratification and targeted treatment particularly challenging (1–4). While attempting to identify oncogenic drivers in TNBC, immunohistochemical and large-scale genomic studies have suggested that EGFR signaling may be frequently activated and associated with poor prognosis (5–8). These findings have long positioned EGFR as an intriguing target in TNBC. Efforts to target EGFR in unselected TNBC patients have, however, yielded low response rates (9–15). This is indicative of possible intrinsic resistance and its underlying mechanisms as a major impediment to more widespread use of EGFR inhibitors in TNBC.

Broad dysregulation of gene expression is one of the hallmarks of cancer, including TNBC, pointing to the potential utility of targeted therapeutics that alter gene regulation (16, 17). Indeed, the development of specific inhibitors targeting multiple key players in transcriptional regulation has provided opportunities for therapeutic interventions (18–20). Cyclin-dependent kinases (CDK) 12 and 13 are well known for regulating transcriptional and posttranscriptional processes, and CDK12 has also recently been shown to play a role in the regulation of cap-dependent translation (21–27). THZ531, a selective inhibitor of CDK12/13, has been reported to suppress expression of genes that support malignant progression and induce apoptosis in cancer cell line models (28, 29). This work and our broadening understanding of CDK12/13's regulation of DNA damage response pathway genes have driven the recent development of these kinases as both biomarkers and therapeutic targets (30–40). However, the functional interactions between CDK12/13 and most major oncogenic signaling pathways have remained largely unexplored.

Motivated by the hypothesis that CDK12/13 may functionally interact with major oncogenic signaling pathways in TNBC, we performed a candidate drug screen to identify synergistic drug combinations between THZ531 and inhibitors targeting possible oncogenic disease drivers. This work led to the unexpected finding that intrinsic resistance to EGFR inhibition in TNBC, a long-standing and unexplained observation, is mediated by CDK12/13. Studies into the mechanism underlying the profound synergy between

Significance

Triple-negative breast cancer (TNBC) is an aggressive and lethal subtype of the disease. For almost two decades, the epidermal growth factor receptor (EGFR) has been speculated to play an important role in disease progression, but clinical trials of EGFR inhibitors have been disappointing, suggesting that these tumors may possess mechanisms of intrinsic resistance. Here, we identify that this resistance is driven by cyclin-dependent kinases 12 and 13 (CDK12/13) and that as such, combination therapies targeting EGFR and CDK12/13 exhibit potent and synergistic activity in TNBC models. This combination therapy functions through a surprising mechanism involving disrupted synthesis and stability of driver oncoproteins. Together, these findings expand our understanding of pathophysiological cell signaling in TNBC and illuminate a promising therapeutic approach.

The authors declare no competing interest.

This article is a PNAS Direct Submission.

[1]Present address: Department of Biosciences and Nutrition, Karolinska Institutet, Stockholm SE-14157, Sweden.

[2]To whom correspondence may be addressed. Email: christopher.nicchitta@duke.edu or kris.wood@duke.edu.

This article contains supporting information online at https://www.pnas.org/lookup/suppl/doi:10.1073/pnas.2221448120/-/DCSupplemental.

Published September 11, 2023.

EGFR and CDK12/13 inhibitors revealed that the stability of driver oncoproteins in TNBC is subject to translation-coupled regulation by these kinases, thereby nominating a mechanistically distinct approach for targeting oncogenic dependencies in this important disease subtype.

Results

CDK12/13 Inhibition Sensitizes TNBC Cells to EGFR Inhibition. As there is no known single, targetable oncogenic driver in TNBC, we designed a panel of inhibitors targeting an array of key molecular pathways that are frequently implicated in cancer cell proliferation, survival, differentiation, and apoptosis. We tested two TNBC cell lines with this panel of inhibitors in the presence versus absence of a low, sublethal dose of THZ531 (*SI Appendix*, Fig. S1*A*). Both TNBC lines were markedly sensitized to the EGFR inhibitors gefitinib and lapatinib, as reflected by 10–100-fold reductions in GI_{50} values in the presence of THZ531 (Fig. 1*A*). Further studies showed consistent THZ531-mediated sensitization to EGFR inhibitors across each member of a panel of eight diverse TNBC cell lines, decreasing their GI_{50} values to the submicromolar range in each case (Fig. 1 *B* and *C*). The sensitization effect was specific to TNBC cell lines and not observed in luminal breast cancer cell lines (BT474 and SK-BR-3) or the immortalized mammary epithelial line, MCF10A (Fig. 1*C*). Long-term combined EGFR and CDK12/13 inhibition suppressed colony formation and cell growth in multiple TNBC cell lines (Fig. 1*D*). Using an established analytic tool—Synergy Finder 2.0 with method selected for the Loewe additivity model and the Bliss independence model, additional quantitative analyses of our drug combination screening

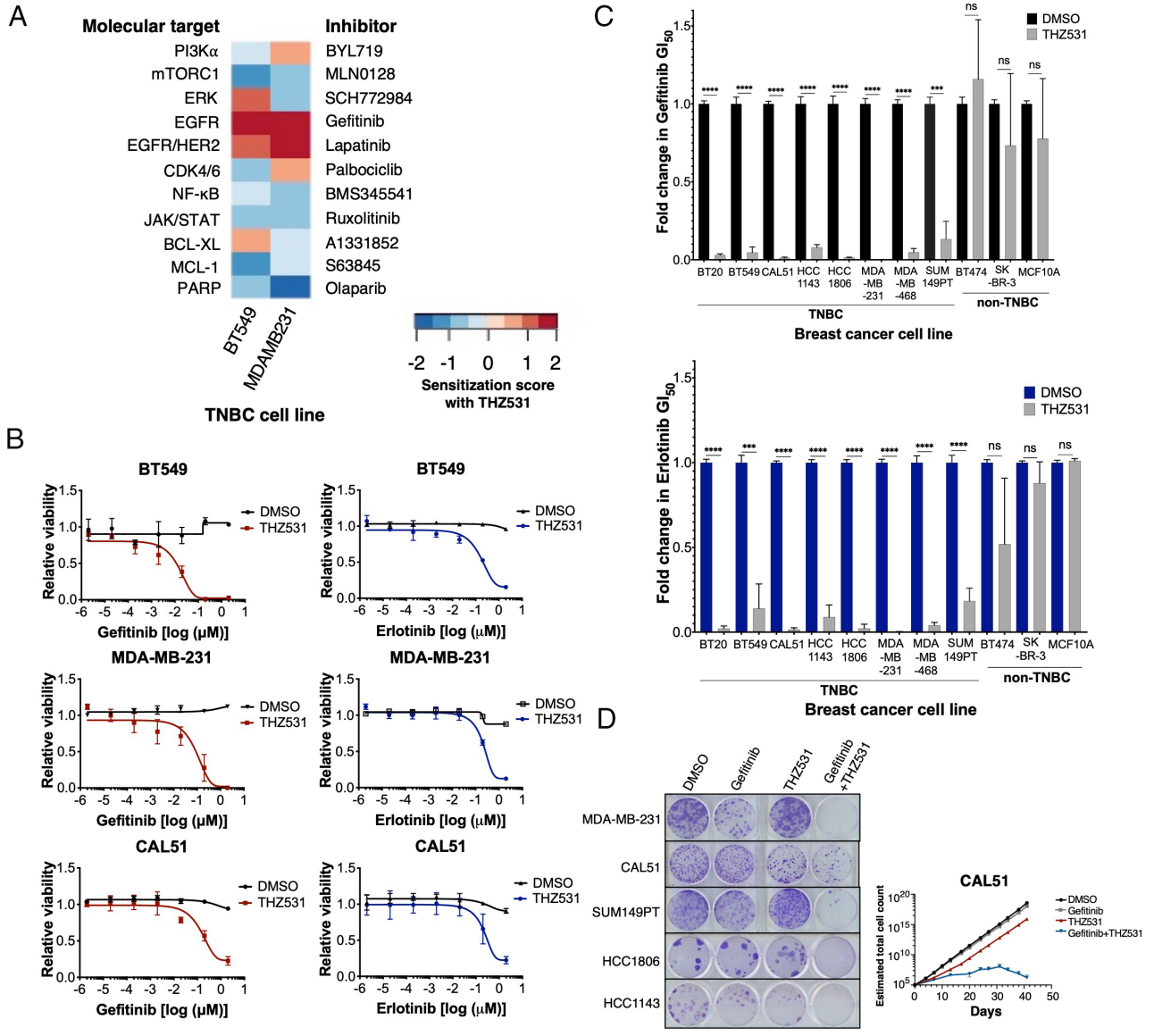

Fig. 1. Sensitization to EGFR inhibition with THZ531 in TNBC cells. (*A*) Heatmap depicting the sensitization scores (ratio of GI_{50} values for the indicated drug in the absence versus presence of THZ531, log_{10} transformed) for a panel of inhibitors targeting potential oncogenic drivers in BT549 and MDA-MB-231 TNBC cell lines. (THZ531 background concentrations were BT549, 50 nM, and MDA-MB-231, 200 nM). (*B*) EGFR inhibitor (gefitinib and erlotinib) dose–response curves in BT549, MDA-MB-231, and CAL51 treated with DMSO control or THZ531 in the background (BT549, 50 nM; MDA-MB-231 and CAL51, 200 nM). (*C*) Fold change in 72 h GI_{50} values for EGFR inhibitors (gefitinib or erlotinib) in the presence of DMSO control or THZ531 in the background across a panel of breast cancer cell lines. (MCF10A is an immortalized, nonmalignant breast epithelial cell line.) Within each cell line, absolute GI_{50} values are normalized to vehicle treatment. (THZ531 background doses: BT549 and SK-BR-3, 50 nM; HCC1143 and HCC1806, 100 nM; BT474 and MDA-MB-468, 150 nM; BT20, CAL51, MDA-MB-231, and MCF10A, 200 nM; SUM149PT, 250 nM). ns = not significant, ***$P \le 0.001$, ****$P \le 0.0001$ by Student's *t* tests; n = 3. Data are mean ± SD of three biological replicates. (*D*) Clonogenic growth assay (MDA-MB-231, CAL51, SUM149PT, HCC1806, and HCC1143) and time-to-progression assay (CAL51) on TNBC cells treated with DMSO, gefitinib, THZ531, or gefitinib +THZ531 (gefitinib at 1 μM; THZ531 doses as in *C*). Representative images and data of n = 3 independent experiments.

data confirmed synergy between EGFR inhibition and THZ531 in multiple TNBC cell lines (*SI Appendix*, Fig. S1*B*) (41–43). To confirm that the effects of THZ531 were through CDK12/13 inhibition, we examined a stereoisomer (THZ531R), and a derivative of THZ531 (THZ532), each of which spare CDK12 and CDK13 (28); neither compound synergized with gefitinib in cell viability studies (*SI Appendix*, Fig. S1*C*). Additionally, we observed that the sensitizing effect of THZ531 was lost in cells expressing a mutant version of CDK12 ($CDK12^{AS}$) (44, 45), generated by endogenous CRISPR-mediated gene editing, that is not inhibited by the drug (*SI Appendix*, Fig. S1*D*). (We note that we were unable to isolate TNBC cells harboring a $CDK13^{AS}$ mutation.) The loss of CDK12 or CDK13 impeded both the toxicity of THZ531 alone as well as THZ531-induced sensitization to gefitinib (*SI Appendix*, Fig. S1*E*), suggesting that inhibition of both CDK12 and CDK13 is required for the observed synergistic effect. Collectively, these findings demonstrate that EGFR is an oncogenic driver in TNBC and that intrinsic resistance to EGFR inhibitors in TNBC can be mitigated by CDK12/13 inhibition.

Concurrent EGFR and CDK12/13 Inhibition Decreases the Levels of Key Oncogenic Proteins in TNBC Cells. The global involvement of CDK12/13 in transcription elongation, mRNA splicing, and intronic polyadenylation (24, 26, 44–46) prompted us to examine the genes whose expression was selectively affected by the drug combination. Using an unbiased transcriptomic approach, we performed RNA-seq analyses in two TNBC cell lines treated with vehicle control, the single agents gefitinib and THZ531, and the combination. Consistent with CDK12/13's role in transcriptional regulation, THZ531 treatment resulted in the differential expression of thousands of genes. However, relatively few genes were further differentially expressed in the combined gefitinib plus THZ531 condition (Fig. 2*A*, *SI Appendix*, Fig. S2*A*, and Dataset S1 *A* and *B*). This result led us to hypothesize that the synergistic activity of the combination therapy may be due, at least in part, to nontranscriptional mechanisms. To examine this hypothesis, we evaluated the levels of key oncogenic proteins in TNBC cells treated with vehicle control, single agents, and the combination. In three TNBC cell lines, combined treatment with gefitinib and THZ531 was accompanied by markedly reduced levels of MYC and MCL-1 proteins (Fig. 2*B*). These proteins are notable, as extensive studies have documented their roles as driver oncoproteins in TNBC (47–60).

MYC Protein Levels Are Suppressed through both Decreased Protein Synthesis and Increased Ubiquitin-Proteasome-Dependent Protein Degradation in EGFR- and CDK12/13-Inhibited Cells. Given the well-established role of MYC as a driver oncoprotein in TNBC (47–57), we sought to understand the basis for its loss following coinhibition of EGFR and CDK12/13. Specifically, we surveyed each step of MYC biogenesis—transcription, translation, and degradation. Direct analysis of *MYC* mRNA transcription using quantitative real-time PCR showed increased mRNA expression in gefitinib plus THZ531 treated cells (*SI Appendix*, Fig. S3*A*), a surprising result given the loss of MYC protein with the same combination. Although previous studies suggested that MYC mRNA levels may be acutely suppressed with CDK12/13 inhibition (28, 37), our data reveal that on the timescale of therapeutic effects,

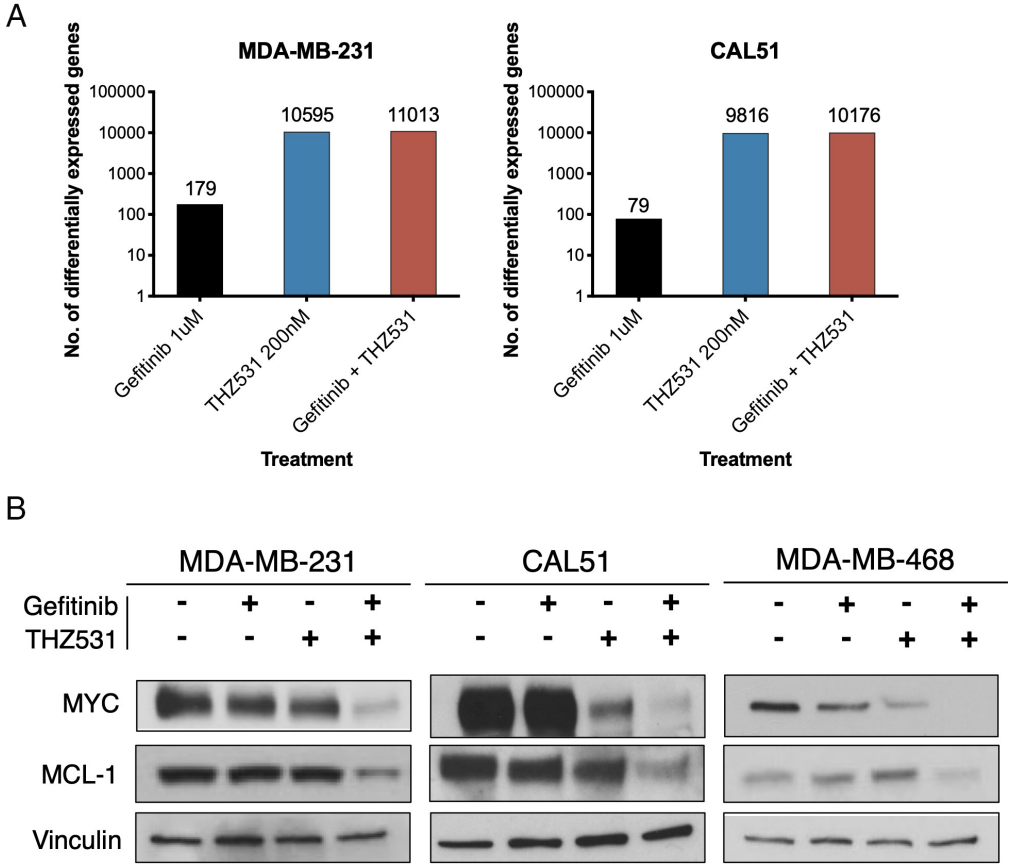

Fig. 2. Concurrent EGFR and CDK12/13 inhibition results in the loss of key oncogenic proteins in TNBC cells. (*A*) Number of differentially expressed genes, assessed by RNA-seq of cells treated with gefitinib (1 μM), THZ531 (200 nM), or the combination, compared to DMSO control, in CAL51 and MDA-MB-231 cells. (*B*) Immunoblot analysis of MYC, MCL-1, and vinculin levels in TNBC cells (MDA-MB-231, CAL51, and MDA-MB-468) treated as indicated (gefitinib at 1 μM; THZ531 doses as in Fig. 1*C*). Representative immunoblot of n = 3 independent experiments.

MYC transcript levels are increased and thus cannot account for the observed reductions in MYC protein levels.

We next examined the effects of gefitinib and THZ531 on mRNA translation using sucrose density gradient polysome profiling. Polysome profiles showed reduced levels of heavy polysomes in cells treated with THZ531 alone and the drug combination, consistent with global suppression in mRNA translation in the drug-treated cells (Fig. 3*A*, boxed polysome fractions). To determine whether the global changes in polysome profiles included reductions in *MYC* mRNA translation, [^{35}S]methionine labeling followed by MYC immunoprecipitation was performed in cells treated with gefitinib+THZ531. As observed in the phosphorimage and normalized quantification, [^{35}S]methionine incorporation into nascent MYC proteins was considerably decreased in the combination-treated versus the vehicle-treated samples (Fig. 3*B*), providing direct evidence of MYC translational suppression in the presence of combined gefitinib and THZ531.

To examine MYC stability in the combination treatment protocol, we performed a cycloheximide chase experiment. MYC protein stability was unaffected by gefitinib but slightly decreased with THZ531 alone and to a greater extent with the combination treatment (Fig. 3*C* and *SI Appendix*, Fig. S3*B*). We further investigated the canonical MYC protein degradation pathway by the ubiquitin–proteasome system. Following MYC protein immunoprecipitation, we observed a substantial increase in MYC ubiquitination in cells treated with gefitinib plus THZ531 (Fig. 3*D* and *SI Appendix*, Fig. S3*C*). Consistent with these data, proteasome inhibition by bortezomib rescued the decline in MYC protein levels seen in the drug combination condition, indicating proteasome-dependent degradation of MYC (Fig. 3*E*). Together, these data demonstrate that the cumulative loss of MYC protein

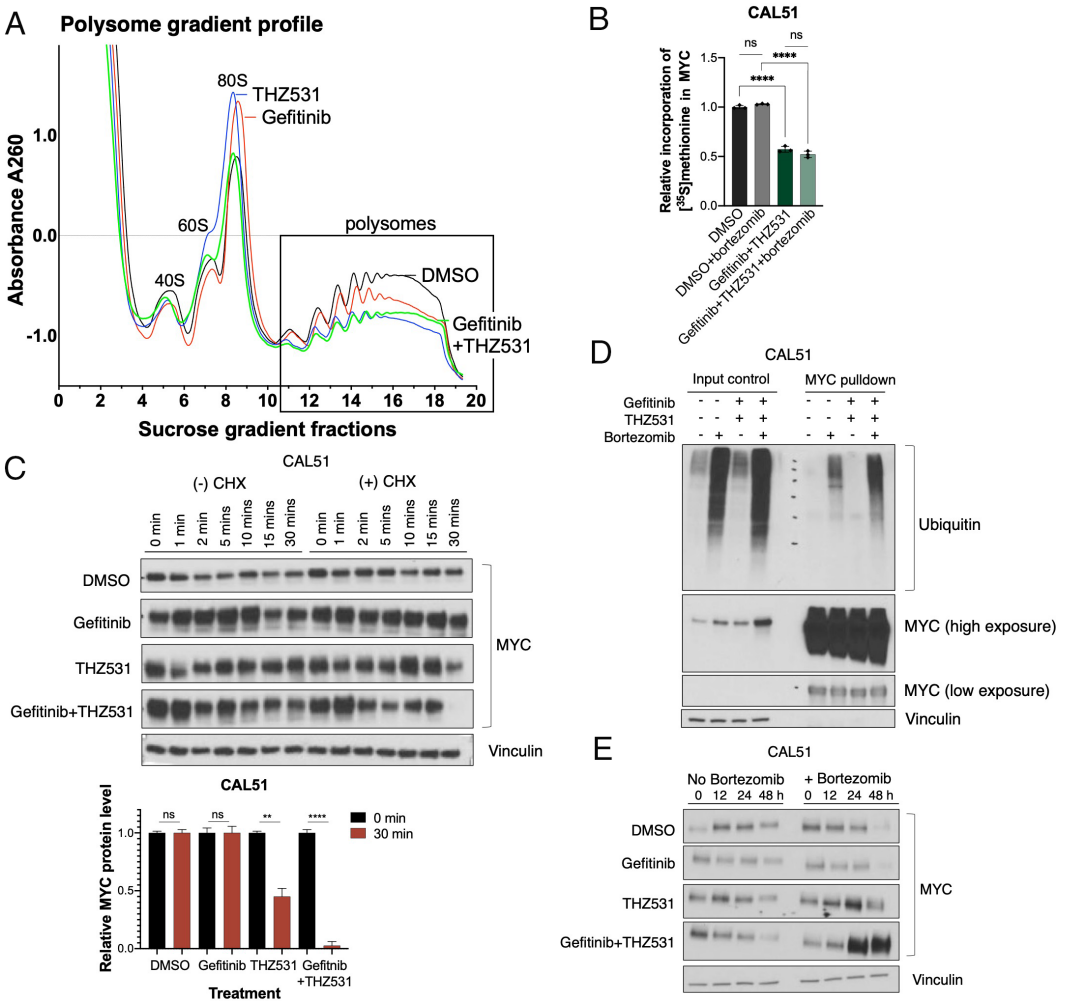

Fig. 3. MYC protein loss is driven by decreased protein synthesis and increased ubiquitin-proteasome-dependent protein degradation. (*A*) Polysome gradient profiles of CAL51 cells treated with DMSO, gefitinib (1 μM), THZ531 (200 nM), or gefitinib + THZ531 for 12 h. Polysome fractions are indicated by the black box. Representative analysis of the polysome distribution of n = 2 independent experiments yielding similar results. (*B*) Relative incorporation of [^{35}S]methionine in MYC protein, determined by phosphorimager analysis and densitometry quantification of immunoblots, following [^{35}S]methionine labeling and MYC protein immunoprecipitation in the absence or presence of proteasome inhibitor, bortezomib (20 nM) in CAL51 cells treated with DMSO or gefitinib (1 μM) + THZ531 (200 nM) for 12 h. ns = not significant, ****$P \le 0.0001$ by Student's *t* tests; n = 3. Data are mean ± SD of three biological replicates. (*C*) Immunoblot analysis of MYC and vinculin over a time course as indicated in the absence or presence of cycloheximide (20 μg/mL) in CAL51 cells treated with DMSO, gefitinib (1 μM), THZ531 (200 nM), or gefitinib + THZ531. Representative immunoblot of n = 3 independent experiments. Relative MYC protein level at time 0 and 30 min with indicated treatment conditions, derived from densitometry quantification of immunoblots from cycloheximide chase experiment of CAL51 cells. ns = not significant, **$P \le 0.01$, ****$P \le 0.0001$ by Student's *t* tests; n = 3. Data are mean ± SD of three independent experiments. (*D*) Immunoblot analysis of ubiquitin, MYC, and vinculin on immunoprecipitated MYC protein and input control in the absence or presence of proteasome inhibitor, bortezomib (20 nM) in CAL51 cells treated with DMSO or gefitinib (1 μM) + THZ531 (200 nM) for 18 h. Representative immunoblot of n = 3 independent experiments yielding similar results. (*E*) Immunoblot analysis of MYC and vinculin protein levels over a time course as indicated in the absence or presence of bortezomib (20 nM) in CAL51 cells treated with DMSO, gefitinib (1 μM), THZ531 (200 nM), or gefitinib + THZ531. Representative immunoblot of n = 3 independent experiments yielding similar results.

following combined EGFR and CDK12/13 inhibition results from suppressed MYC translation and increased MYC protein degradation.

EGFR and CDK12/13 Inhibition Synergistically Decrease MYC Protein Stability through Their Regulation of 4E-BP1 Phosphorylation. It was recently reported that CDK12 acts as a positive regulator of cap-dependent translation through direct phosphorylation of the mRNA 5′ cap-binding repressor, 4E-BP1 (25). This led us to consider whether the suppression of MYC protein synthesis following combined EGFR and CDK12/13 inhibition occurs via the dephosphorylation of 4E-BP1. In line with this hypothesis, we observed dephosphorylation of the four well-established 4E-BP1 phosphosites (T37, T46, S65, and T70) with the drug combination (Fig. 4*A*). This indicates that combined CDK12/13 and EGFR inhibition prevented phosphorylation of 4E-BP1, thus retaining cap-binding on mRNA and suppressing cap-dependent mRNA translation, consistent with the polysome profile data illustrated in Fig. 3*A*.

Work in model systems has demonstrated that alterations in protein synthesis rates can affect the stability of nascent polypeptides (61–64). To understand whether 4E-BP1-dependent suppression of cap-dependent translation drives the reduction in MYC stability, we used a 3' UTR-targeted shRNA to suppress the expression of endogenous 4E-BP1, then simultaneously expressed a dominant negative, nonphosphorylatable mutant of 4E-BP1 (T37A, T46A, S65A, and T70A) under doxycycline-responsive control (*SI Appendix*, Fig. S4*A*). In this experimental system, MYC half-life was substantially suppressed, indicating that suppression of MYC synthesis rate is alone sufficient to destabilize the protein (Fig. 4*B*). Further, we observed that the nonphosphorylatable mutant 4E-BP1 blocked the ability of gefitinib + THZ531 to

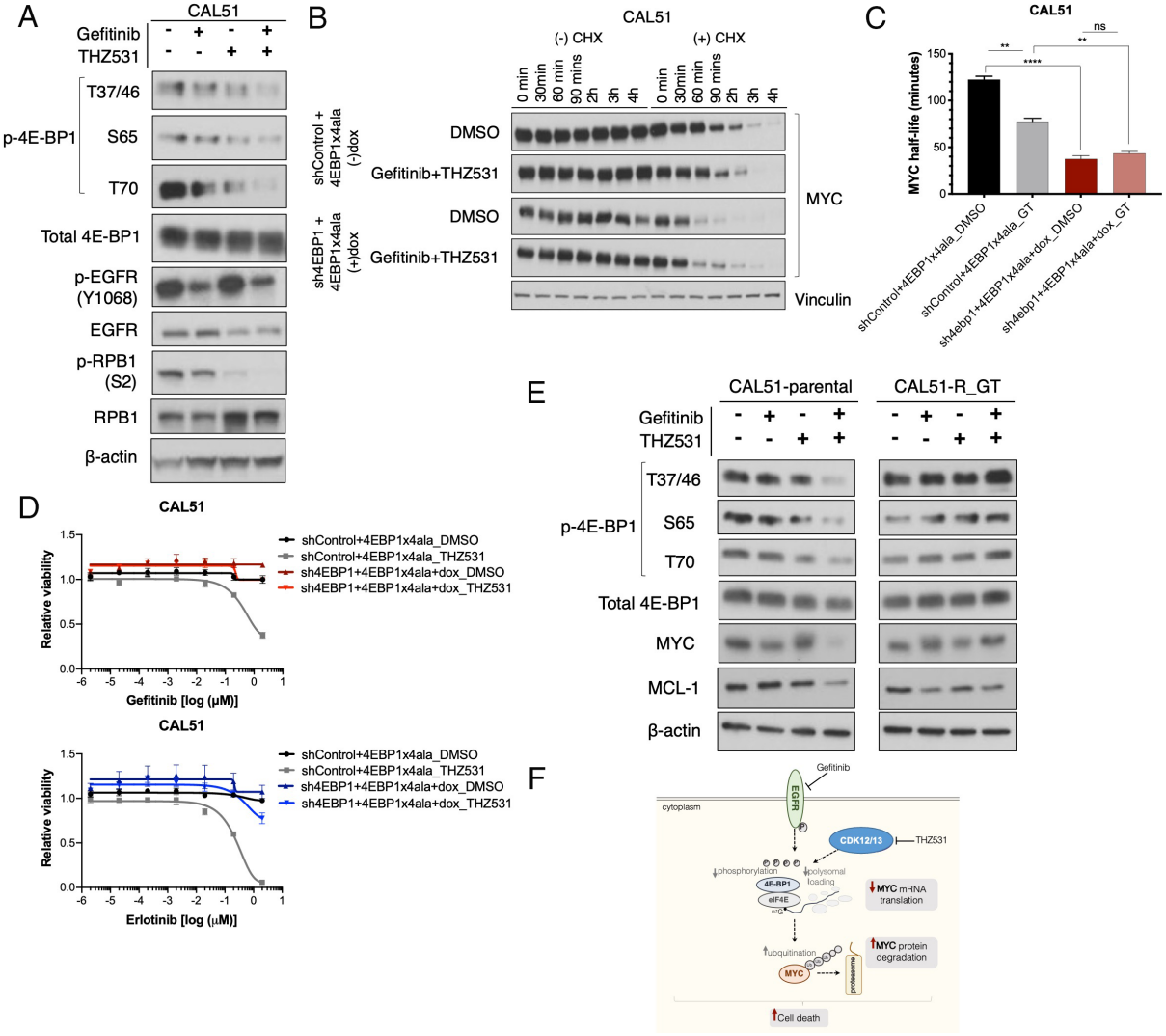

Fig. 4. Combined EGFR and CDK12/13 inhibition destabilizes MYC protein and drives cell death through regulation of 4E-BP1 phosphorylation. (*A*) Immunoblot analysis of 4E-BP1 phosphorylation at T37/46, S65, and T70, total 4E-BP1, phospho-EGFR (Y1068), total EGFR, phospho-RPB1 (S2), total RPB1, and β-actin in CAL51 cells treated with DMSO, gefitinib (1 μM), THZ531 (200 nM), or gefitinib + THZ531 for 24 h. Representative immunoblot of n = 3 independent experiments yielding similar results. (*B*) Immunoblot analysis of MYC and vinculin over a time course as indicated in the absence or presence of cycloheximide (20 μg/mL) in CAL51 cells expressing a doxycycline-inducible, nonphosphorylatable 4E-BP1 mutant and a 3′ UTR-targeted sh4EBP1 construct (to remove endogenous 4E-BP1), treated with DMSO or gefitinib (1 μM) + THZ531 (200 nM). Representative immunoblot of n = 3 independent experiments. (*C*) MYC protein half-life derived from densitometric quantification of immunoblots from cycloheximide chase experiment of CAL51 4E-BP1-manipulated derivatives in *B*. ns = not significant, $^{**}P \leq 0.01$, $^{****}P \leq 0.0001$ by Student's *t* tests; n = 3. Data are mean ± SD of three independent experiments. (*D*) EGFR inhibitor (gefitinib and erlotinib) dose–response curves in CAL51 4E-BP1-manipulated derivatives treated with or without THZ531 (200 nM) in the background. (*E*) Immunoblot analysis of 4E-BP1 phosphorylation at T37/46, S65 and T70, total 4E-BP1, MYC, MCL-1, and β-actin in gefitinib + THZ531 (GT)-resistant and parental CAL51 cells treated with DMSO, gefitinib (1 μM), THZ531 (200 nM), or gefitinib + THZ531 for 12 h. Representative immunoblot of n = 3 independent experiments. (*F*) Summarized mechanistic model of cooperative regulation of 4E-BP1 activity with combined EGFR and CDK12/13 inhibition leads to MYC destabilization in TNBC cells.

further destabilize MYC, suggesting that the drug combination destabilizes MYC through its effects on 4E-BP1 phosphorylation (Fig. 4 *B* and *C*).

Beyond its effects on MYC, the overall cytotoxic effect of the combination therapy was also dependent on 4E-BP1, as replacement of endogenous 4E-BP1 with the nonphosphorylatable mutant blocked the cellular response to the drug combination (Fig. 4*D*). Consistent with this finding, TNBC cells cultured chronically in media containing gefitinib and THZ531 until they developed resistance were insensitive to drug-induced suppression of 4E-BP1 phosphorylation as well as MYC and MCL-1 levels (Fig. 4*E* and *SI Appendix*, Fig. S4 *B* and *C*). Consequently, an expected and pronounced dependence on MYC was observed in these TNBC cells (*SI Appendix*, Fig. S4*D*). Together, these findings demonstrate that combined EGFR and CDK12/13 inhibition leads to MYC destabilization and cell death through the cooperative regulation of 4E-BP1 activity (Fig. 4*F*).

CNOT1 Is Required for Combination Therapy–Induced MYC Translational Suppression, MYC Degradation, and Cell Death. To gain further insight into the mechanisms underlying the biological activity of the combination therapy, we performed genome-wide CRISPR/Cas9-based loss-of-function screens in cells treated with vehicle control or gefitinib + THZ531 (Fig. 5*A*). We focused our analysis on genes whose knockouts were enriched in the combination-treated arm, as genes scoring in this group can be interpreted as being required for the full activity of the combination therapy. Analysis of the screen revealed that multiple CNOT family gene knockouts were enriched in cells treated with gefitinib + THZ531 (Fig. 5*B* and Datasets S2 and S3). The CCR4-NOT complex, which is comprised of multiple CNOT family proteins, is reported to function in posttranscriptional mRNA deadenylation, translational quality control, and protein ubiquitylation (65–72). Among the CNOT family genes, CNOT1, a central scaffolding component of the CCR4-NOT complex, was the top-scoring gene in our screen. CNOT1 knockout led to a nearly complete rescue of the cooperativity between EGFR and CDK12/13 inhibitors as well as the overall toxicity of the drug combination (Fig. 5 *C* and *D*). CNOT1 loss also rendered cells insensitive to drug-induced loss of both 4E-BP1 phosphorylation and consequent MYC and MCL-1 protein loss (Fig. 5*E*). MYC loss in CNOT1 knockdown cells expectedly hindered colony formation, consistent with the notion that these cells maintain MYC dependence (*SI Appendix*, Fig. S4*E*). Further, CNOT1 protein expression was lost in cells with naturally evolved resistance to the combination therapy (Fig. 5*F*), suggesting that it may be responsible for the resistance of these cells to drug-induced 4E-BP1 dephosphorylation and death.

Discussion

The finding over a decade ago of EGFR hyperactivation in TNBC and its correlation with aggressive disease, chemoresistance, and poor prognosis positioned EGFR as a prime therapeutic target in this disease subset. However, the subsequent observation of poor clinical responses to EGFR inhibitors in TNBC patients dampened enthusiasm for this therapeutic target and raised a fundamental question: is EGFR a driver of TNBC pathogenesis whose importance is obscured by mechanisms of intrinsic resistance, or is it simply a bystander signaling event (14)? Here, we resolve this question, demonstrating that the inhibition of CDK12/13 reveals an exquisite dependence of diverse TNBC models on EGFR signaling. Further, these studies reveal that EGFR and CDK12/13 cooperate to drive TNBC not through transcriptional regulation, but rather by promoting the synthesis and associated stabilization of key driver oncoproteins, including MYC (47–57). As such, the coupled nature of protein synthesis and stability, which has been well-explored in model systems (61–64), is shown here to underlie the therapeutic activity of a promising anticancer strategy.

Several key open questions remain. First, while the drug combination under study clearly functions through the modulation of 4E-BP1-regulated, coupled protein synthesis and stability, the relative contributions of decreased oncoprotein synthesis versus decreased stability to the observed toxicity have not been clarified. Further, the extent to which EGFR- and/or CDK12/13-regulated transcriptional events or proteasome modulation may template the observed mechanism of action has not been resolved. Second, a number of reports have described cooperativity between EGFR blockade and inhibition of receptor tyrosine kinase-PI3K-mTOR signaling in TNBC (73–79). A recent report also demonstrated that the effects of EGFR inhibition can be potentiated through blockade of Elongator complex-mediated MCL-1 translation (15). It remains to be determined whether these processes regulate, or are regulated by, CDK12/13. Third, although this study identifies MYC and MCL-1 protein loss as likely key events downstream of combined EGFR and CDK12/13 inhibition, unbiased proteomic approaches may reveal additional TNBC driver oncoproteins that are similarly affected. Fourth, the precise mechanisms by which the CCR4-NOT impacts EGFR- and CDK12/13-regulated 4E-BP1 activity and downstream oncoprotein stability remain to be defined. The CCR4-NOT complex has been shown to regulate mRNA metabolism directly through miRNA-mediated deadenylation of mRNAs and translation by interacting with translational regulators such as eIF4E and DDX6 and blocking the decapping machinery (65–71). Further, it also functions in the ubiquitination of nascent, translationally arrested polypeptides and the maintenance of 26S proteasome integrity (66, 72), suggesting that its regulatory roles in the phenomena under study here may be multifactorial, including at transcriptional level. Finally, the full therapeutic potential of combined EGFR and CDK12/13 inhibition has not been evaluated in preclinical animal models because THZ531 is not amenable to in vivo administration. Interestingly, our findings suggest that as-yet undefined criteria must be met in order to achieve sensitization to EGFR blockade by CDK12/13 inhibition, as in our hands, neither dual knockdown of CDK12/13 nor an alternative CDK12/13 inhibitor, SR-4835, phenocopied the effects of THZ531 (38), despite clear evidence that THZ531 functions in a CDK12/13-dependent manner (*SI Appendix*, Fig. S1 *C–E*). The inability of CDK12/13 knockdown to phenocopy THZ531 may be explained by the fact that CDK12/13 function as components of larger complexes, and loss of the proteins may destabilize or alter the makeup of these complexes in ways that are not phenocopied by kinase inhibition, a result observed in other contexts by our group and others (80, 81). Additionally, kinase inhibitors work immediately, whereas genetic knockdowns occur over longer periods of time, which potentially allows for compensatory effects. The fact that EGFR inhibitor sensitization by THZ531 is not phenocopied by SR-4835 may be attributable to the fact that the latter compound is a noncovalent, ATP-competitive inhibitor that is mechanistically distinct from the covalent, allosteric THZ-531. SR-4835 is also likely to exhibit a different spectrum of off-target effects than THZ531. Ongoing and future studies are expected to provide mechanistic clarity to explain these observations and precisely define the criteria that must be met in order for an in vivo bioavailable CDK12/13 inhibitor to potentiate the activity of EGFR blockade.

In summary, by revealing a long-debated EGFR dependence in TNBC, we have identified a therapeutic approach that functions through an unexpected mechanism of action and holds promising

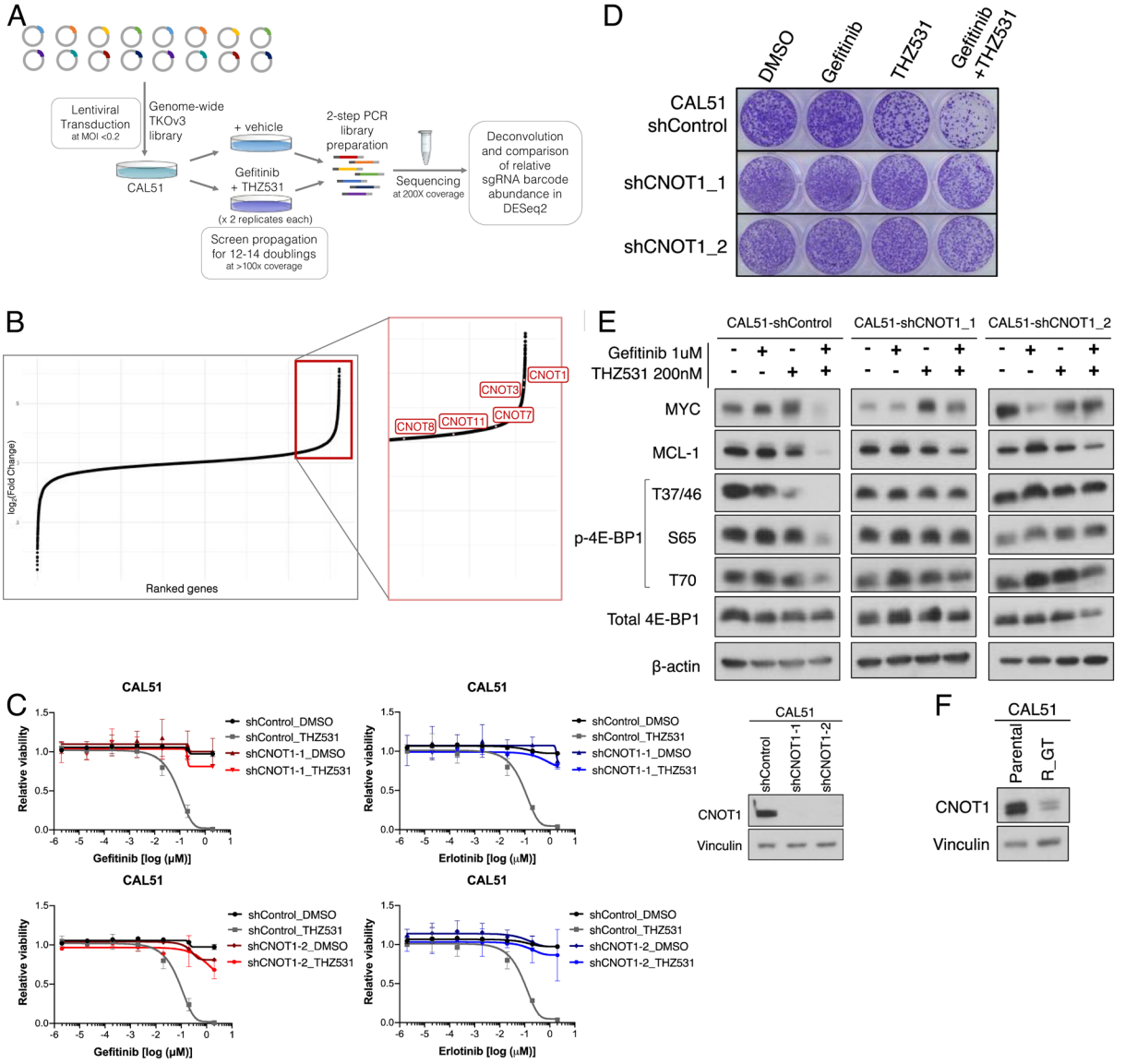

Fig. 5. CNOT1 is required for combination therapy–induced translational suppression, MYC degradation, and cell death. (*A*) Schematic overview of genome-wide CRISPR positive selection screen. (*B*) Gene-level representation of screen results, ranked by $\log_2$(fold change). Cluster of CNOT family genes (highlighted in red) are enriched among those knockouts (boxed) enriched in the gefitinib+THZ531 combination-treated population. (*C*) EGFR inhibitor (gefitinib and erlotinib) dose-response curves in CAL51 cells expressing shControl or each of two independent shRNAs targeting CNOT1, treated with or without THZ531 200 nM in the background. Immunoblot analysis of CNOT1 and vinculin in CAL51 cells expressing the indicated shRNAs (*Right*). (*D*) Clonogenic growth assay of CAL51 cells expressing the indicated shRNAs and treated with DMSO, gefitinib (1 μM), THZ531 (200 nM), or gefitinib + THZ531. Representative images of n = 3 independent experiments. (*E*) Immunoblot analysis of MYC, MCL-1, phospho-4E-BP1 (T37/46, S65, T70), total 4E-BP1, and β-actin in CAL51 expressing the indicated shRNAs and treated with DMSO, gefitinib (1 μM), THZ531 (200 nM), or gefitinib + THZ531 for 24 h. Representative immunoblot of n = 3 independent experiments. (*F*) Immunoblot analysis of CNOT1 and vinculin in GT-resistant and DMSO-control CAL51 cells. Representative immunoblot of n = 3 biological replicates.

translational potential for the treatment of this difficult-to-treat disease subtype.

Materials and Methods

Cell lines, Reagents, and Inhibitors. BT20, BT474, BT549, CAL51, HCC1143, HCC1806, HeLa, MCF10A, MDA-MB-231, MDA-MB-468, SK-BR-3, and SUM149PT cell lines were purchased from Duke University Cell Culture Facility or American Type Culture Collection. HeLa-CDK12^{AS} was kindly provided by Dr. Arnold Greenleaf (Duke University). All cell lines were authenticated using short tandem repeat profiling by the Duke University DNA Analysis Facility and tested negative for *mycoplasma* contamination using MycoAlert™ PLUS *Mycoplasma* Detection kit (Lonza). All cell lines were cultured at 37 °C in 5% CO2. See *SI Appendix*, Table S1 for specific culture media.

Drugs were purchased from SelleckChem or Apexbio Technology. THZ531R and THZ532 were generously gifted by Nathanael Gray (Harvard University, Dana-Farber Cancer Institute).

Evolving Drug-Resistant CAL51 Cell Line. To evolve resistance to the gefitinib+THZ531 combination in vitro, CAL51 cells were exposed to the combined drugs with increasing concentrations. Cells were first drugged at a dose approximately equal to their GI_{75} value (concentration for 25% of maximal inhibition of cell viability). As CAL51 cells were insensitive to gefitinib, an arbitrary starting dose of 500 nM was selected, while 50 nM of THZ531 was used. The growth rate was monitored by cell counts with passaging every 3 to 5 d. Once the growth rate was stabilized, the concentration of each drug was increased until the maximal preset synergistic dose of 1 μM gefitinib and 200 nM THZ531 was reached, yielding CAL51-R_GT (CAL51, resistant to gefitinib + THZ531). A paired vehicle control

was cultured with DMSO-containing media in parallel (CAL51-parental). Resistant cells were achieved over 8 wk with gradual dose increments.

GI_{50} and Sensitization Assay. Cells were seeded in 96-well plates at a density of 3,000 to 5,000 cells per well and treated with a 10-fold serial dilution of indicated drug. Calculated drug dilution series yield final drug concentrations starting with vehicle (DMSO) at 0, 0.000002, 0.00002, 0.0002, 0.002, 0.02, 0.2, and 2 μM. The CellTiter-Glo luminescent viability assay (Promega) was used to measure cell viability after 72 h drug incubation. Luminescence from each specific well of each plate was measured using a Tecan plate reader (Infinite M1000 PRO). Each treatment condition was performed in triplicate per plate, and the presented data represent three technical replicates. Relative viability was calculated by normalizing raw luminescence values to vehicle-treated wells. GI_{50} values were considered as the dose at which cell viability equates to 50% of DMSO-treated viability and determined by fitting each individual experiment to a four-parameter logistic drug-response curve using GraphPad/Prism9 software.

For two-drug combinations, the concentration of a second background drug was kept constant across all wells. Sensitization scores were calculated using GI_{50} values with vehicle versus the second background drug as fold change and $\log_{10}$ transformed; thus, sensitization scores >0 will indicate increased sensitivity to the first serially diluted drug. GI_{50} assays were first performed singly to obtain dose–response curves for THZ531 with each cell line. Background doses for THZ531 were then chosen based on the curves at doses yielding no less than 80% viability to ensure adequate cellular representation of response to the first serially diluted drug.

Background doses of THZ531 were 50 nM for BT549 and SK-BR-3, 100 nM for HCC1143 and HCC1806, 150 nM for BT474 and MDA-MB-468, 200 nM for BT20, CAL51, MCF10A and MDA-MB-231, and 250 nM for SUM149PT.

Loewe and Bliss Synergy Scores Calculation. To quantitatively assess synergy, GI_{50} assays were first performed for each inhibitor (e.g., gefitinib or erlotinib) with a range of four or more fixed concentrations of the second background drug (e.g., THZ531 0, 50, 100, and 200 nM). Relative cell viability was calculated as described earlier. Data were tabulated according to SynergyFinder 2.0 User Documentation and uploaded on the web application for analysis (41). Four-parameter logistic regression (LL4) was selected for the curve-fitting algorithm and outlier detection was turned on (82). The Loewe and Bliss methods (42, 43) were selected, separately, for synergy calculation with the 'Correction' option switched on to eliminate detected outlier and apply a baseline correction method on the single drug–dose responses.

Clonogenic Growth Assay. To measure long-term effects of inhibitors and their combination on cell growth, cells were seeded at 500 cells/well in 12-well tissue culture plates or 1,000 cells/well in six-well tissue culture plates in complete media. For cells expressing shRNA(s) or CRISPR construct(s), cells were seeded after at least 3 d posttransduction. Twenty-four h after seeding, media were aspirated, and drugs were added into fresh media to each specific well. Media and drugs were refreshed every 5 d, and assays were cultured for 10 to 15 d. Drug media were then removed, and plates were fixed and stained with 0.5% w/v crystal violet in 80% v/v methanol solution for 20 min at room temperature. Plates were rinsed with distilled water and scanned.

Time-to-Progression Assay. To evaluate the relative ability of treatments to delay the reemergence of logarithmic cell growth in vitro, cells were plated in triplicate wells in six-well plates at 1E5 cells per well in normal growth media. After 24 h, the growth media were replaced with the indicated treatment. At the time points indicated, the cells were lifted with 0.25% trypsin (Life Technologies) and counted using a Z2 Coulter Particle Count and Size Analyzer (Beckman Coulter, Pasadena, CA). For each replicate in each treatment condition, all cells were centrifuged at 1,200 rpm for 5 min, supernatants were removed, cell pellets were resuspended in fresh media, and then, up to 1E5 cells were replated in a well with fresh treatment. This procedure was repeated every 5 to 7 d for about 8 to 10 wk, depending on the kinetics of resistance and cell growth. Weekly growth rates (μ) were calculated from the number of cells plated the previous week (N0) and the number counted the current week (N) according to the formula $\ln N = \ln N0 + \mu * t$; where t is elapsed time. These growth rates were then used to estimate the total cell number.

Immunoblotting and Antibodies. Immunoblotting was performed as previously described (83). Briefly, cells were resuspended in RIPA lysis buffer (Sigma-Aldrich) supplemented with protease and phosphatase inhibitors (ThermoFisher), incubated on ice for 10 min, and then disrupted with QiaShredder columns (Qiagen), followed by centrifugation of cell lysates at 13,000 rpm for 2 min at 4 °C. Protein in the whole cell lysates was quantified using the Bradford method, normalized, and combined with 4× Laemmli Sample Buffer (Bio-Rad). Proteins were run on Mini-PROTEAN TGX Stain-Free Precast 4 to 20% Gels (Bio-Rad) and transferred to PVDF membrane (TransBlot Turbo, Bio-Rad). Membranes were blocked and probed in 5% BSA overnight at 4 °C with primary antibodies as follows, β-actin (1:2,000, CST#4970), CDK12 (1:1,000, CST#11973), CDK13 (1:1,000, ThermoFisher #PA5-67681), c-MYC (1:500, Ab#32072), CNOT1 (1:1,000, CST#44613), EGFR (1:1,000, CST#2232), phospho-EGFR (Tyr1068) (1:1,000, CST#2234), HSP90 (1:1,000, CST #4877), MCL-1 (1:1,000, CST#94296), Rpb1CTD (1:1,000, CST#2629), phospho-RPB1(Ser2) (1:1,000, CST#13499), 4E-BP1(1:1,000, CST#9644), phospho-4E-BP1 (Thr37/46) (1:1,000, CST#2855), phospho-4E-BP1 (Ser65) (1:1,000, CST#9451), phospho-4E-BP1 (Thr70) (1:1,000, CST#13396), ubiquitin (1:1,000, CST#3936), and vinculin (1:2,000, CST#13901). HRP-linked anti-rabbit (CST#7074) and anti-mouse (CST #7076) secondary antibodies were used at a 1:5,000 dilution in 5% milk in PBS-T at room temperature. Quantification of immunoblots was performed where indicated with ImageJ software (84, 85). Background measurement was subtracted, and band intensity was normalized to loading control intensity. See *SI Appendix*, Table S2 for antibodies.

Immunoprecipitation. Cells were seeded in 15-cm plates, treated with DMSO or indicated drugs for 18 h, to yield at least 1 mg of total protein for immunoprecipitation. All subsequent steps were performed on ice. At the time of harvest, cells were washed with PBS, pelleted (3,000 rpm, 4 °C, 5 min), resuspended, and incubated on a rotator for 1 h, 4 °C, in IP buffer (150 mM NaCl, 0.5% NP-40, 20 mM EDTA, 1 mM dithiothreitol (DTT), and 40 mM Tris–HCl, pH7.4) supplemented with protease/ phosphatase inhibitor cocktail (ThermoFisher). After lysis was completed, lysates were clarified at 13,000 rpm, 4 °C, 20 min. Protein was quantified using the Bradford method and normalized to the lowest protein amount among the samples. Input controls were also saved, and samples were prepared by combining with 4× Laemmli Sample Buffer (Bio-Rad) accordingly. 2 to 4 μg of primary antibodies (c-MYC, Ab#32072) or appropriate isotype control were added to the clarified cell extracts and incubated overnight on a rotator at 4 °C. 40 μL/sample of recombinant Protein-G-Sepharose-4B beads (ThermoFisher) was washed thrice with IP buffer and added to each sample for equilibration on a rotator for 4 h, 4 °C. Immunoprecipitates were collected by centrifugation at 3,000 rpm for 5 min at 4 °C. The bead pellets were washed for a total of five times. After the last wash, immunoprecipitated proteins were eluted with 4× Laemmli Sample Buffer, vortexed briefly, and heated at 95 °C for 5 min. Samples were collected (13,000 rpm, 2 min), subjected to SDS-PAGE, and transferred to PVDF membrane as described above.

RNA-Seq Sample Preparation and Analysis. RNA sequencing was performed with External RNA Controls Consortium (ERCC) spike-in normalization as previously described (86). Briefly, CAL51 and MDA-MB-231 cells were seeded in 10-cm plates and incubated in media with DMSO or indicated drugs for 12 h, in triplicates. Cell counts were determined using C-Chip disposable hemocytometers (Bulldog bio, DHC-N01) and equalized across all samples before lysis and RNA extraction. Total RNA from 1E6 cells per replicate was isolated using the RNeasy96 kit (Qiagen). ERCC ExFoldRNA Spike-in Control Mixes (Invitrogen #4456740) (4 μL/sample, diluted at 1:100, ERCC User Guide, table 4) were added after the cell lysis step. The extraction was then continued according to the manufacturer's instructions and eluted in 50 μL nuclease-free water. Total RNA was quantified using the Qubit™ RNA Broad Range Assay kit (Invitrogen) and analyzed on Agilent 4,200 TapeStation for integrity. Samples with the RNA Integrity Number above 9.0 and normalized to 500 ng total RNA were selected for library preparation using the TruSeq® stranded mRNA sample prep kit (Illumina, #20020595). After library preparation, samples were quantified using Qubit™ assay, checked fragment sizes on Agilent 4,200 TapeStation, normalized, and pooled. Libraries were sequenced on the Illumina HiSeq 2,000 sequencing system using 50-bp single-end reads at the Duke University Genome Sequencing Facility.

Sequences were processed using Trimmomatic v0.32 (87) and reads that were 20 nt or longer after trimming were filtered for further analysis. Reads were aligned using the alignment tool STAR v2.4.1a (88) following the proposed 2-pass strategy to first identify a splice junction database to improve the overall mapping quality. Alignment was performed to GRCh38/hg38 of the human genome

and transcriptome with ERCC synthetic spike-in RNA sequences (Annotations from product webpage manuals, https://assets.thermofisher.com/TFS-Assets/LSG/manuals/cms_095046.txt) appended for mapping. The TPM (transcripts per million) was computed for each mapped gene and synthetic spike-in RNA using RSEM v1.2.25 (89). Differential expression analysis was performed using DESeq2 v1.22.0 (90) running on R (v3.5.1). Briefly, raw counts were imported and filtered to remove genes with low or no expression, that is, keeping genes having two or more counts per million in two or more samples. Filtered counts were then normalized with the DESeq function, using the counts for the ERCC spike-in probes to estimate the size factors. In order to find significant differentially expressed genes, the nbinomWaldTest was used to test the coefficients in the fitted Negative Binomial GLM using the previously calculated size factors and dispersion estimates. Genes having a Benjamini–Hochberg false discovery rate less than 0.05 were considered significant (unless otherwise indicated). Differential gene expression was tested for all possible drug pairwise comparisons within each cell line, for example, single drug versus DMSO control, combination versus DMSO control, combination versus single drug, and so on.

Quantitative Real-Time PCR. Cell counts were determined and normalized across all samples before lysis. RNA was extracted using the RNeasy Mini kit (Qiagen). After the cell lysis step, samples were spiked-in with the ERCC spike-in controls (2 μL/sample, diluted 1:100, Invitrogen #4456740) and treated with on-column DNase digestion according to the manufacturer's specifications (Qiagen). RNA purity and concentration were measured by absorbance at 260nm (A_{260}/A_{280}). cDNAs were reverse-transcribed using the SuperScript™ VILO™ cDNA Synthesis kit (Invitrogen) with 100 ng to 1 μg of RNA template as directed by the manufacturer's protocol. qRT-PCRs were carried out in triplicates using the TaqMan assay (Applied Biosystems) and CFX96 or CFX384 Touch Real-Time PCR Detection System according to manufacturers' recommendations (Bio-Rad). Average cycle threshold (C_t) values were calculated for each gene, and the maximum C_t value was set at 40 cycles. Average C_t values of technical replicates were normalized to the exogenous spike-in or reference gene, ERCC-00096 or *GAPDH* respectively, and relative gene expression was determined using the comparative $\Delta\Delta C_t$ method. Average and SD were results of at least three independent experiments. Specific TaqMan gene expression assay IDs were as follows: ERCC-00096 (Ac03459927_a1), *GAPDH* (Hs02786624_g1), and *MYC* (Hs99999003_m1).

Sucrose Density Gradient Sedimentation of Polysomes. CAL51 cells were seeded in 10-cm plates and cultured until 80 to 85% confluence at the point of harvest. Drug treatments with DMSO or indicated drugs were performed over a 12 h period prior to processing. Sucrose density gradients (15 to 50% sucrose in 200 mM KCl, 25 mM K-HEPES, pH 7.4, 15 mM $MgCl_2$, 0.2 mM cycloheximide, 1 mM DTT, and 10 U/mL RNaseOut™) were prepared prior to cell harvesting. All subsequent steps were performed on ice. Untreated or treated cells were washed twice with ice-cold PBS and lysed on ice for 10 min with 1 mL/ plate lysis buffer (200 mM KCl, 15 mM $MgCl_2$, 1% NP-40, 0.5% sodium deoxycholate, 0.2 mM cycloheximide, 1 mM DTT, 40 U/mL RNaseOUT™, 1× protease inhibitor, and 25 mM K-HEPES, pH 7.4). Lysates were clarified at 13,000 ×g, 4 °C, 10 min. Clarified supernatants were overlaid onto sucrose gradients. The samples were centrifuged in a swinging-bucket rotor (SW41 Ti, Beckman) at 35,000 rpm, 4 °C, for 3 h. Sucrose gradients were fractionated on a Teledyne-ISCO density gradient fractionation system with continuous A_{260} monitoring. Photomultiplier output was continuously sampled and converted to digital values with a TracerDAQ™ A/D converter.

[^{35}S]methionine Labeling. CAL51 cells were seeded in six-well plates, grown to 80 to 85% confluence, and subsequently treated with DMSO or indicated drugs. After 12 h of vehicle or drug incubation, cells were washed twice with PBS and methionine-starved by incubation in serum-supplemented methionine-free media (Gibco) for 30 min at 37 °C. Cells were labeled with 150 μCi/mL [^{35}S] methionine (Perkin-Elmer, NEG772002MC) in methionine-free media for 45 min. [^{35}S] methionine incorporation was terminated by washing cells twice with 100 μg/mL cycloheximide (Sigma-Aldrich)in serum-free methionine-free media, incubating for 10 min at 37 °C for the second wash, followed by two washes with 100 μg/mL cycloheximide in PBS. Cells were then lysed with IP buffer on ice for 10 min. Samples were precleared by addition of rabbit IgG isotype control (Ab #172730) and Protein-G-Sepharose-4B beads for 1 h at 4 °C. MYC immunoprecipitation was performed as described above. Following washing, immunoprecipitated proteins were eluted in 4× Laemmli Sample Buffer (Bio-Rad), vortexed briefly, and heated at 95 °C for 5 min. Two microliters of each sample was added to 3 mL of liquid scintillation liquid, and [^{35}S] radioactivity was measured and recorded. The remaining sample volume was resolved by SDS-PAGE and transferred to PVDF membrane as described above. Membranes were exposed on a phosphorimaging screen overnight and visualized on Amersham™ Typhoon™ NIR Biomolecular Imager (GE Healthcare). See *SI Appendix*, Table S2 for antibodies.

CRISPR Homology-Directed Repair (HDR) Generation of CAL51 CDK12^{AS} Mutant Clones. Cells harboring a CDK12^{AS} mutation were generated using the CRISPR/Cas9 system and HDR as previously described in ref. (45). Briefly, 5E5 cells were transfected in a six-well plate with DNA for the PX458 plasmid (Addgene ID 48138) encoding a Cas9 nuclease and sgRNA targeting the CDK12 gatekeeper residue (4 μg) along with an HDR donor template containing the sequence of the CDK12^{AS} mutation (1 μg), utilizing 8 μL Lipofectamine 3,000 (ThermoFisher) supplemented with 8 μL P3000 (ThermoFisher) reagent in concordance with the product literature. Cells were cultured in the presence of Alt-R™ HDR Enhancer V2 (IDT #10007910), collected, and sorted based on GFP expression via FACS to generate single-cell clones. Clones were screened via PCR amplification of the CDK12 gatekeeper locus from gDNA isolated using the DNeasy Blood & Tissue Kit (Qiagen) followed by Sanger sequencing. Heterozygous CDK12^{AS} mutation was confirmed in the selected clone. See *SI Appendix*, Table S2 for sgRNA sequences.

Cloning of CRISPR and shRNA Constructs. CRISPR constructs were cloned using published methods (91, 92) using characterized sgRNAs from the TKOv3 genome-wide library (93). Detailed cloning steps were as previously described (94). In brief, unique 20-mer sgRNA inserts targeting genes of interest were synthesized by CustomArray with flanking sequence adaptors. The synthetic oligo (diluted 1:100) was amplified using NEB Phusion Hotstart Flex PCR master mix and array primers. Amplified inserts were bead cleaned up at a 1.8× ratio by volume (Axygen, AxyPrep™ Mag PCR Clean-up kit). Ninety microliters of magnetic beads was added to 50 μL of each PCR product, vortexed vigorously, incubated at room temperature for 10 min, and separated on a magnetic tube stand. Clear liquid was aspirated from the magnetic beads, and beads were washed three times with freshly prepared 70% ethanol. After the final wash, PCR products were eluted in molecular-grade water. lentiCRISPRv2 (Addgene ID 52961), PX458 (Addgene ID 48138), or FUW-U6-enhanced gRNA-hUbC-mCherry-PuroR [kindly provided by Charlie Gersbach (Duke University)] was digested by Esp3I (BsmBI) (NEB) and size selected by 1% agarose gel electrophoresis and extraction. Linearized gRNA expression vector were then annealed with clean array amplified sgRNA oligos by Gibson assembly reaction. The reaction mixture was then transformed by chemical or electroporation method into Stbl3 (ThermoFisher) or E. cloni 10G (Lucigen) competent cells, respectively. Transformed cells were recovered and spread on LB-ampicillin plates for overnight incubation. Single colonies were picked, cultured overnight in liquid LB, and extracted using the plasmid miniprep kit (Qiagen). Plasmid DNA sequences were checked using Sanger sequencing (Eton Bioscience) for sgRNA inserts to confirm successful cloning. See *SI Appendix*, Table S2 for sgRNA sequences.

Glycerol stocks for shRNA targeting genes of interest and bacterial stab cultures of plasmids were obtained from the Duke Functional Genomics Core Facility and Addgene Plasmid Repository, respectively. Inoculants from glycerol stocks or stab culture were cultured overnight in liquid LB at 37 °C, and plasmids were extracted using the Plasmid miniprep kit (Qiagen). See *SI Appendix*, Table S2 for shRNA identity, TRC number and target sequences, and plasmid Addgene ID.

Lentivirus Production and Transduction. Lentivirus production was adapted from ref. (92). HEK293FT cells were grown to ~80% confluency in 10-cm or six-well plates, for 10 mL or 2 mL final viral media harvest, respectively, and transfection reagents were scaled according to seeding area. For a 10-cm plate, 3.5 – 4E6 cells were seeded and incubated for 24 h (37 °C, 5% CO2). Transfection reagents were prepared in Opti-MEM™ reduced serum medium (Gibco) and performed using 94.2 μL Lipofectamine 2,000 (ThermoFisher), 103.6 μL PLUS™ reagent (ThermoFisher), 8.2 μg psPAX2, 5.4 μg pMD2.G, and 10.7 μg construct DNA. The mixture was incubated at room temperature for 5 min and gently added to the HEK293FT cells for 4 h incubation (37 °C, 5% CO2). The medium was then replaced with prewarmed harvest media (DMEM 30% FBS). Forty-eight h after the start of the transfection, the lentivirus supernatant was collected and filtered (0.45 μm). Transductions were conducted directly at the time of lentivirus harvest

or freshly thawed from frozen aliquots. 0.5 to 1 mL of virus media and polybrene (1 μg/mL) were added to cells seeded in a six-well plate in 1 to 1.5 mL of growth media. Cells were spinfected at 2,250 rpm, 1 h, room temperature (25 °C), and incubated overnight (37 °C, 5% CO2). Twenty-four h posttransduction, cells were selected by puromycin (2 μg/mL) for 48 h.

Pooled Genome-Wide CRISPR Positive Selection Screen and Analysis. The TKOv3 pooled library was obtained from Addgene (Addgene ID 90294) and amplified as previously described (92, 93). Lentivirus production of the TKOv3 library was scaled up and conducted as described above. CAL51 cells were seeded into 6-well plates at a density of 0.5E6 cells per well and transduced at an MOI less than 0.2. A total of 60E6 cells were transduced in 24× six-well plates. Twenty-four h posttransduction, cells were selected by puromycin (2 μg/mL) for 48 h. Puromycin-selected cells were collected and counted to confirm at least 100× library coverage. Transduced cells were propagated in puromycin-containing media for a total of 7 d and split into vehicle (DMSO) and gefitinib (750 nM) + THZ531 (100 nM) combination treatment conditions in duplicates. The screen was conducted over a total of 3 wk, for approximately 15 cell doublings. Cells were counted and passaged with replenished drug every 3 d. Each treatment condition and replicate was represented by a minimum of 10E6 cells to maintain at least 100× library coverage (>100 cells per unique sgRNA) during each split throughout the screen. A total of 12E6 cells were collected at 48 h after puromycin exposure, screen initiation (t_0), and at every passage till screen termination (t_{final}). DNA was extracted from cell pellets (DNeasy Blood & Tissue Kit, Qiagen) and stored at −80 °C until completion of screens. Samples were further processed for sequencing as previously described (91). Screen libraries were sequenced on the Illumina NovaSeq 6,000 sequencing system (50-bp, single-end reads) at the Duke University Genome Sequencing Facility to achieve 20 million reads total per sample (~200 reads per guide).

Pooled samples were matched by barcoded reads, and guide-level counts were computed using bcSeq (v1.12.0) Bioconductor package (95) in the R (v3.5.1) programming environment. As the screen was designed for positive selection, resistance to gefitinib+THZ531 combination was determined by evaluating differential guide compositions between vehicle control (DMSO) and combo-treated (GT) cell populations at t_{final}. Cells that survived the GT combo were enriched with guides targeting genes that we coined 'resistor' genes and are required for the drug synergistic activities. Differential analysis was carried out using the DESeq2 (v1.22.0) Bioconductor package in the R (v3.5.1) programming environment. Out of the 18,053 genes in the TKOv3 library, 29 genes (0.16%) were excluded due to low counts. Enrichment effects in combo-treated arm were expressed as $\log_2$(fold-change) for GT versus DMSO (vehicle-control as the denominator).

Quantification and Statistical Analysis. Statistical analyses were performed in Prism9 (GraphPad) software or R (v3.5.1) (https://www.r-project.org/). All results are shown as mean ± SD. *P* Values were determined using unpaired, two-tailed Student's *t* tests and considered significant at a threshold of <0.05, unless otherwise stated.

Data, Materials, and Software Availability. The RNA-seq data have been deposited in Gene Expression Omnibus (GEO) accession number GSE221475 (96) and are publicly available as of the date of publication. RNA-seq counts table after normalization with synthetic ERCC spike-in-RNA is available in Dataset S1 *A* and *B*. Raw counts table for the TKOv3 positive selection screen of CAL51 cells treated with DMSO or gefitinib+THZ531 combination is available in Dataset S2. Analyzed screen data are available in Dataset S3. All study data are included in the article and/or supporting information.

ACKNOWLEDGMENTS. We thank the members of the C.V.N. and K.C.W. laboratories as well as Sarah Sammons, James Alvarez, Shanhu Hu, David Moebius, Susan Henry, John Carulli, and Claudio Chuaqui for their valuable support and feedback on the manuscript. We thank Arno Greenleaf for helpful discussions and for providing $CDK12^{AS}$-expressing HeLa cells. We thank Charlie Gersbach for providing lentiviral gRNA expression vector. We thank Tim Haystead and David Loiselle for facilitating the [^{35}S]methionine labeling experiment. Duke University School of Medicine and Duke Cancer Institute start-up funds (K.C.W.). NIH grant R01CA207083 (K.C.W.). NIH grant RO1GM139480 (C.V.N.). Department of Defense Breast Cancer Research Program grant W81XWH1910414 (K.C.W.). Department of Defense Breast Cancer Research Program grant W81XWH1610703 (K.C.W.). Agency for Science, Technology and Research, Singapore (NSS-PhD to H.X.A.).

Author affiliations: [a]Department of Pharmacology & Cancer Biology, Duke University School of Medicine, Durham, NC 22710; [b]Duke-National University of Singapore Medical School, Singapore 169857, Singapore; [c]Department of Surgery, Duke University School of Medicine, Durham, NC 22710; [d]Duke Center for Genomic and Computational Biology, Department of Biostatistics and Bioinformatics, Duke University School of Medicine, Durham, NC 27708; [e]Department of Cell Biology, Duke University School of Medicine, Durham, NC 22710; [f]Department of Biostatistics and Bioinformatics, Duke University School of Medicine, Durham, NC 27708; and [g]Bioinformatics Shared Resources, Duke Cancer Institute, Duke University Medical Center, Durham, NC 27705

Author contributions: H.X.A., N.S., X.L.D., A.L., C.G.C.-S., L.C.B., T.E.R., C.V.N., and K.C.W. designed research; H.X.A., N.S., X.L.D., A.L., C.G.C.-S., H.M.H., H.K., L.C.B., and Q.C. performed research; A.B., J.L., Z.S., I.C.M., T.E.R., C.V.N., and K.C.W. contributed new reagents/analytic tools; H.X.A., N.S., X.L.D., A.L., C.G.C.-S., H.M.H., H.K., Q.C., A.B., J.L., Z.S., and I.C.M. analyzed data; and H.X.A., C.V.N., and K.C.W. wrote the paper.

1. B. D. Lehmann *et al.*, Identification of human triple-negative breast cancer subtypes and preclinical models for selection of targeted therapies. *J. Clin. Invest.* **121**, 2750–2767 (2011).
2. B. D. Lehmann *et al.*, Refinement of triple-negative breast cancer molecular subtypes: Implications for neoadjuvant chemotherapy selection. *PLoS One* **11**, e0157368 (2016).
3. W. D. Foulkes, I. E. Smith, J. S. Reis-Filho, Triple-negative breast cancer. *N. Engl. J. Med.* **363**, 1938–1948 (2010).
4. R. Dent *et al.*, Triple-negative breast cancer: Clinical features and patterns of recurrence. *Clin. Cancer Res.* **13**, 4429–4434 (2007).
5. H. S. Park *et al.*, High EGFR gene copy number predicts poor outcome in triple-negative breast cancer. *Mod. Pathol.* **27**, 1212–1222 (2014).
6. Cancer Genome Atlas Network, Comprehensive molecular portraits of human breast tumours. *Nature* **490**, 61–70 (2012).
7. K. A. Hoadley *et al.*, EGFR associated expression profiles vary with breast tumor subtype. *BMC Genomics* **8**, 258 (2007).
8. T. O. Nielsen *et al.*, Immunohistochemical and clinical characterization of the basal-like subtype of invasive breast carcinoma. *Clin. Cancer Res.* **10**, 5367–5374 (2004).
9. J. Baselga *et al.*, Phase II and tumor pharmacodynamic study of gefitinib in patients with advanced breast cancer. *J. Clin. Oncol.* **23**, 5323–5333 (2005).
10. G. Fountzilas *et al.*, Paclitaxel and carboplatin as first-line chemotherapy combined with gefitinib (IRESSA) in patients with advanced breast cancer: A phase I/II study conducted by the hellenic cooperative oncology group. *Breast Cancer Res. Treat.* **92**, 1–9 (2005).
11. L. A. Carey *et al.*, TBCRC 001: Randomized phase II study of cetuximab in combination with carboplatin in stage IV triple-negative breast cancer. *J. Clin. Oncol.* **30**, 2615–2623 (2012).
12. J. Baselga *et al.*, Randomized phase II study of the anti-epidermal growth factor receptor monoclonal antibody cetuximab with cisplatin versus cisplatin alone in patients with metastatic triple-negative breast cancer. *J. Clin. Oncol.* **31**, 2586–2592 (2013).
13. B. Corkery, J. Crown, M. Clynes, N. O'Donovan, Epidermal growth factor receptor as a potential therapeutic target in triple-negative breast cancer. *Ann. Oncol.* **20**, 862–867 (2009).
14. R. Ali, M. K. Wendt, The paradoxical functions of EGFR during breast cancer progression. *Signal Transduct. Target. Ther.* **2**, 16042 (2017).
15. P. Cruz-Gordillo, M. E. Honeywell, N. W. Harper, T. Leete, M. J. Lee, ELP-dependent expression of MCL1 promotes resistance to EGFR inhibition in triple-negative breast cancer cells. *Sci. Signal.* **13**, eabb9820 (2020).
16. D. Hanahan, R. A. Weinberg, Hallmarks of cancer: The next generation. *Cell* **144**, 646–674 (2011).
17. Y. Wang *et al.*, CDK7-dependent transcriptional addiction in triple-negative breast cancer. *Cell* **163**, 174–186 (2015).
18. J. E. Bradner, D. Hnisz, R. A. Young, Transcriptional addiction in cancer. *Cell* **168**, 629–643 (2017).
19. A. Augert, D. MacPherson, Treating transcriptional addiction in small cell lung cancer. *Cancer Cell* **26**, 783–784 (2014).
20. C. L. Christensen *et al.*, Targeting transcriptional addictions in small cell lung cancer with a covalent CDK7 inhibitor. *Cancer Cell* **26**, 909–922 (2014).
21. K. Liang *et al.*, Characterization of human cyclin-dependent kinase 12 (CDK12) and CDK13 complexes in C-terminal domain phosphorylation, gene transcription, and RNA processing. *Mol. Cell Biol.* **35**, 928–938 (2015).
22. C. A. Bösken *et al.*, The structure and substrate specificity of human Cdk12/Cyclin K. *Nat. Commun.* **5**, 3505 (2014).
23. A. K. Greifenberg *et al.*, Structural and functional analysis of the Cdk13/Cyclin K complex. *Cell Rep.* **14**, 320–331 (2016).
24. S. J. Dubbury, P. L. Boutz, P. A. Sharp, CDK12 regulates DNA repair genes by suppressing intronic polyadenylation. *Nature* **564**, 141–145 (2018).
25. S. H. Choi *et al.*, CDK12 phosphorylates 4E-BP1 to enable mTORC1-dependent translation and mitotic genome stability. *Genes Dev.* **33**, 418–435 (2019).
26. S. H. Choi, S. Kim, K. A. Jones, Gene expression regulation by CDK12: A versatile kinase in cancer with functions beyond CTD phosphorylation. *Exp. Mol. Med.* **52**, 762–771 (2020).
27. A. P. Chirackal Manavalan *et al.*, CDK12 controls G1/S progression by regulating RNAPII processivity at core DNA replication genes. *EMBO Rep.* **20**, e47592 (2019).
28. T. Zhang *et al.*, Covalent targeting of remote cysteine residues to develop CDK12 and CDK13 inhibitors. *Nat. Chem. Biol.* **12**, 876–884 (2016).
29. M. Zeng *et al.*, Targeting MYC dependency in ovarian cancer through inhibition of CDK7 and CDK12/13. *Elife* **7**, e39030 (2018).

30. G. Lui, C. Grandori, C. J. Kemp, CDK12: An emerging therapeutic target for cancer. *J. Clin. Pathol.* **71**, 957–962 (2018).
31. Y. M. Wu *et al.*, Inactivation of CDK12 delineates a distinct immunogenic class of advanced prostate cancer. *Cell* **173**, 1770–1782.e14 (2018).
32. H. J. Choi *et al.*, CDK12 drives breast tumor initiation and trastuzumab resistance via WNT and IRS1-ErbB-PI3K signaling. *EMBO Rep.* **20**, e48058 (2019).
33. J. Chou, D. A. Quigley, T. M. Robinson, F. Y. Feng, A. Ashworth, Transcription-associated cyclin-dependent kinases as targets and biomarkers for cancer therapy. *Cancer Discov.* **10**, 351–370 (2020).
34. H. Liu, K. Liu, Z. Dong, Targeting CDK12 for cancer therapy: Function, mechanism, and drug discovery. *Cancer Res.* **81**, 18–26 (2020).
35. D. Blazek *et al.*, The Cyclin K/Cdk12 complex maintains genomic stability via regulation of expression of DNA damage response genes. *Genes Dev.* **25**, 2158–2172 (2011).
36. A. B. Iniguez *et al.*, EWS/FLI confers tumor cell synthetic lethality to CDK12 inhibition in ewing sarcoma. *Cancer Cell* **33**, 202–216.e6 (2018).
37. M. Krajewska *et al.*, CDK12 loss in cancer cells affects DNA damage response genes through premature cleavage and polyadenylation. *Nat. Commun.* **10**, 1757 (2019).
38. V. Quereda *et al.*, Therapeutic targeting of CDK12/CDK13 in triple-negative breast cancer. *Cancer Cell* **36**, 545–558.e7 (2019).
39. W. Abida *et al.*, Non-BRCA DNA damage repair gene alterations and response to the parp inhibitor rucaparib in metastatic castration-resistant prostate cancer: Analysis from the phase II TRITON2 study. *Clin. Cancer Res.* **26**, 2487–2496 (2020).
40. C. Wang *et al.*, CDK12 inhibition mediates DNA damage and is synergistic with sorafenib treatment in hepatocellular carcinoma. *Gut* **69**, 727–736 (2020).
41. A. Ianevski, A. K. Giri, T. Aittokallio, SynergyFinder 2.0: Visual analytics of multi-drug combination synergies. *Nucleic Acids Res.* **48**, W488–W493 (2020).
42. C. I. Bliss, The toxicity of poisons applied jointly. *Ann. App. Biol.* **26**, 585–615 (1939).
43. S. Loewe, The problem of synergism and antagonism of combined drugs. *Arzneimittelforschung* **3**, 286–290 (1953).
44. B. Bartkowiak, C. M. Yan, E. J. Soderblom, A. L. Greenleaf, CDK12 activity-dependent phosphorylation events in human cells. *Biomolecules* **9**, 634 (2019).
45. Z. Fan *et al.*, CDK13 cooperates with CDK12 to control global RNA polymerase II processivity. *Sci Adv.* **6**, eaaz5041 (2020).
46. A. L. Greenleaf, Human CDK12 and CDK13, multi-tasking CTD kinases for the new millenium. *Transcription* **10**, 91–110 (2019).
47. Broad DepMap, Data from "DepMap 19Q3 Public". 10.6084/m9.figshare.9201770.v2. Accessed 1 October 2019.
48. M. Ghandi *et al.*, Next-generation characterization of the cancer cell line encyclopedia. *Nature* **569**, 503–508 (2019).
49. A. Goga, D. Yang, A. D. Tward, D. O. Morgan, J. M. Bishop, Inhibition of CDK1 as a potential therapy for tumors over-expressing MYC. *Nat. Med.* **13**, 820–827 (2007).
50. D. Horiuchi *et al.*, MYC pathway activation in triple-negative breast cancer is synthetic lethal with CDK inhibition. *J. Exp. Med.* **209**, 679–696 (2012).
51. D. Horiuchi *et al.*, PIM1 kinase inhibition as a targeted therapy against triple-negative breast tumors with elevated MYC expression. *Nat. Med.* **22**, 1321–1329 (2016).
52. T. Y. Hsu *et al.*, The spliceosome is a therapeutic vulnerability in MYC-driven cancer. *Nature* **525**, 384–388 (2015).
53. R. Camarda *et al.*, Inhibition of fatty acid oxidation as a therapy for MYC-overexpressing triple-negative breast cancer. *Nat. Med.* **22**, 427–432 (2016).
54. K. M. Lee *et al.*, MYC and MCL1 cooperatively promote chemotherapy-resistant breast cancer stem cells via regulation of mitochondrial oxidative phosphorylation. *Cell Metab.* **26**, 633–647.e7 (2017).
55. N. Klauber-DeMore, B. A. Schulte, G. Y. Wang, Targeting MYC for triple-negative breast cancer treatment. *Oncoscience* **5**, 120–121 (2018).
56. N. Zhao *et al.*, Pharmacological targeting of MYC-regulated IRE1/XBP1 pathway suppresses MYC-driven breast cancer. *J. Clin. Invest.* **128**, 1283–1299 (2018).
57. J. Rohrberg *et al.*, MYC dysregulates mitosis, revealing cancer vulnerabilities. *Cell Rep.* **30**, 3368–3382.e7 (2020).
58. E. A. Bowling *et al.*, Spliceosome-targeted therapies trigger an antiviral immune response in triple-negative breast cancer. *Cell* **184**, 384–403.e21 (2021).
59. C. M. Goodwin, O. W. Rossanese, E. T. Olejniczak, S. W. Fesik, Myeloid cell leukemia-1 is an important apoptotic survival factor in triple-negative breast cancer. *Cell Death Differ.* **22**, 2098–2106 (2015).
60. D. Merino *et al.*, Synergistic action of the MCL-1 inhibitor S63845 with current therapies in preclinical models of triple-negative and HER2-amplified breast cancer. *Sci. Transl. Med.* **9**, eaam7049 (2017).
61. K. C. Stein, J. Frydman, The stop-and-go traffic regulating protein biogenesis: How translation kinetics controls proteostasis. *J. Biol. Chem.* **294**, 2076–2084 (2019).
62. E. M. Sontag, R. S. Samant, J. Frydman, Mechanisms and functions of spatial protein quality control. *Annu. Rev. Biochem.* **86**, 97–122 (2017).
63. O. Brandman, R. S. Hegde, Ribosome-associated protein quality control. *Nat. Struct. Mol. Biol.* **23**, 7–15 (2016).
64. C. Joazeiro, Mechanisms and functions of ribosome-associated protein quality control. *Nat. Rev. Mol. Cell Biol.* **20**, 368–383 (2019).
65. Y. T. Shirai, T. Suzuki, M. Morita, A. Takahashi, T. Yamamoto, Multifunctional roles of the mammalian CCR4–NOT complex in physiological phenomena. *Front. Genet.* **5**, 286 (2014).
66. J. E. Miller, J. C. Reese, Ccr4–Not complex: The control freak of eukaryotic cells. *Crit. Rev. Biochem. Mol. Biol.* **47**, 315–333 (2012).
67. H. Mathys *et al.*, Structural and biochemical insights to the role of the CCR4–NOT complex and DDX6 ATPase in microRNA repression. *Mol. Cell* **54**, 751–765 (2014).
68. Y. Chen *et al.*, A DDX6-CNOT1 complex and W-binding pockets in CNOT9 reveal direct links between miRNA target recognition and silencing. *Mol. Cell* **54**, 737–750 (2014).
69. A. Cooke, A. Prigge, M. Wickens, Translational repression by deadenylases. *J. Biol. Chem.* **285**, 28506–28513 (2010).
70. A. Kamenska *et al.*, The DDX6-4E-T interaction mediates translational repression and P-body assembly. *Nucleic Acids Res.* **44**, 6318–6334 (2016).
71. S. Ozgur *et al.*, Structure of a human 4E-T/DDX6/CNOT1 complex reveals the different interplay of DDX6-binding proteins with the CCR4–not complex. *Cell Rep.* **13**, 703–711 (2015).
72. O. O. Panasenko, M. A. Collart, Not4 E3 ligase contributes to proteasome assembly and functional integrity in part through Ecm29. *Mol. Cell. Biol.* **31**, 1610–1623 (2011).
73. A. El Guerrab, M. Bamdad, Y. J. Bignon, F. Penault-Llorca, C. Aubel, Co-targeting EGFR and mTOR with gefitinib and everolimus in triple-negative breast cancer cells. *Sci. Rep.* **10**, 6367 (2020).
74. K. S. You, Y. W. Yi, S. J. Kwak, Y. S. Seong, Inhibition of RPTOR overcomes resistance to EGFR inhibition in triple-negative breast cancer cells. *Int. J. Oncol.* **52**, 828–840 (2018).
75. A. Simiczyjew *et al.*, Combination of EGFR inhibitor lapatinib and MET inhibitor foretinib inhibits migration of triple negative breast cancer cell lines. *Cancers* **10**, 335 (2018).
76. N. Verma *et al.*, Targeting of PYK2 synergizes with EGFR antagonists in basal-like TNBC and circumvents HER3-associated resistance via the NEDD4-NDRG1 axis. *Cancer Res.* **77**, 86–99 (2017).
77. J. J. Tao *et al.*, Antagonism of EGFR and HER3 enhances the response to inhibitors of the PI3K-Akt pathway in triple-negative breast cancer. *Sci. Signal.* **7**, ra29 (2014).
78. J. Sohn *et al.*, cMET activation and EGFR-directed therapy resistance in triple-negative breast cancer. *J. Cancer* **5**, 745–753 (2014).
79. S. Lev, Targeted therapy and drug resistance in triple-negative breast cancer: The EGFR axis. *Biochem. Soc. Trans.* **48**, 657–665 (2020).
80. C. Vogel, E. M. Marcotte, Insights into the regulation of protein abundance from proteomic and transcriptomic analyses. *Nat. Rev. Genet.* **13**, 227–232 (2012).
81. D. P. Nussbaum *et al.*, Mediator kinase inhibition impedes transcriptional plasticity and prevents resistance to ERK/MAPK-targeted therapy in KRAS-mutant cancers. bioRxiv [Preprint] (2022). https://www.biorxiv.org/content/10.1101/2022.09.17.508384v1 (Accessed 28 August 2023).
82. A. Ianevski *et al.*, Prediction of drug combination effects with a minimal set of experiments. *Nat. Mach. Intell.* **1**, 568–577 (2019).
83. K. R. Singleton *et al.*, Melanoma therapeutic strategies that select against resistance by exploiting MYC-driven evolutionary convergence. *Cell Rep.* **21**, 2796–2812 (2017).
84. C. T. Rueden *et al.*, Image J2: ImageJ for the next generation of scientific image data. *BMC Bioinformatics* **18**, 529 (2017).
85. C. A. Schneider, W. S. Rasband, K. W. Eliceiri, NIH image to ImageJ: 25 years of image analysis. *Nat. Met.* **9**, 671–675 (2012).
86. J. Lovén *et al.*, Revisiting global gene expression analysis. *Cell* **151**, 476–482 (2012).
87. A. M. Bolger, M. Lohse, B. Usadel, Trimmomatic: A flexible trimmer for Illumina sequence data. *Bioinformatics* **30**, 2114–2120 (2014).
88. A. Dobin *et al.*, STAR: Ultrafast universal RNA-seq aligner. *Bioinformatics* **29**, 15–21 (2013).
89. B. Li, C. N. Dewey, RSEM: Accurate transcript quantification from RNA-Seq data with or without a reference genome. *BMC Bioinformatics* **12**, 323 (2011).
90. M. I. Love, W. Huber, S. Anders, Moderated estimation of fold change and dispersion for RNA-seq data with DESeq2. *Genome Biol.* **15**, 550 (2014).
91. O. Shalem *et al.*, Genome-scale CRISPR-Cas9 knockout screening in human cells. *Science* **343**, 84–87 (2014).
92. J. Joung *et al.*, Genome-scale CRISPR-Cas9 knockout and transcriptional activation screening. *Nat. Protoc.* **12**, 828–863 (2017).
93. T. Hart *et al.*, Evaluation and design of genome-wide CRISPR/SpCas9 knockout screens. *G3 (Bethesda)* **7**, 2719–2727 (2017).
94. K. H. Lin *et al.*, Systematic dissection of the metabolic-apoptotic interface in AML reveals heme biosynthesis to be a regulator of drug sensitivity. *Cell Metab.* **29**, 1217–1231.e7 (2019).
95. J. Lin *et al.*, bcSeq: An R package for fast sequence mapping in high-throughput shRNA and CRISPR screens. *Bioinformatics* **34**, 3581–3583 (2018).
96. H.X. Ang *et al.*, Cooperative regulation of coupled oncoprotein synthesis and stability in triple-negative breast cancer by EGFR and CDK12/13. NCBI GEO. https://www.ncbi.nlm.nih.gov/geo/query/acc.cgi. Deposited 22 December 2022.